Supplementary Information for "Kerr-cat Qubit Operations Below the Fault-tolerant Threshold"

1 Measurement Hardware, Device Layout and Device Parameters

The Kerr-cat qubit is implemented on a planar superconducting circuit device. The equivalent circuit diagram of the device with the measurement wiring diagram is shown in Fig. 1a, and the false-color micrograph of the device chip is shown in Fig. 1b. The key component of the Kerr-cat qubit device, SNAIL nonlinear oscillator (yellow), consists of two SNAILs shunted by a coplanar capacitor, where each SNAIL is formed by three large Josephson junctions connected in parallel with a small Josephson junction, as shown in Fig, 1c. A readout resonator (dark green) is capacitively coupled to the SNAIL nonlinear oscillator with a dispersive shift χ to enable the quantum nondemolition readout of the Kerr-cat qubit, and a Purcell filter (light green) is introduced between the readout resonator and the readout port (pink) to engineer the desired readout resonator decay rate κ_r with suppressed Purcell decay. We engineered two microwave ports to deliver the microwave efficiently without introducing too much Purcell decay. On the one hand, a control port (orange) is weakly coupled to the SNAIL nonlinear oscillator to deliver the single-photon drive for the continuous $Z(\theta)$ gates. On the other hand, a pump port (purple) with a bandblock filter is strongly coupled to the SNAIL nonlinear oscillator to deliver the two-photon stabilization drive and the cat-qubit readout (CQR) drive, where the bandblock filter strongly suppressed the Purcell decay from this port by blocking the signal around the qubit frequency. Detailed description of the bandblock filter can be found in our previous work[1].

We characterize the Kerr-cat qubit with the microwave network shown in Fig. 1a, where we neglect some filters, amplifiers and attenuators for simplicity and clarity, and a detailed wiring diagram can be found in our previous work[1]. The modulation and demodulation of the microwave drive is implemented by two local oscillators, frequency mixers, and a frequency doubler. A readout local oscillator (LO) at readout resonator frequency ω_R is introduced to demodulate the readout signal from the readout port (pink) of the device, and a qubit LO at SNAIL nonlinear oscillator frequency ω_Q is split into three parts to generate the control, readout and stabilization drives. The first one is directly fed into the IQ mixer to generate the single-photon drive, which is connected to the weakly coupled port (orange) of the device. The second one is fed into a frequency doubler to make its frequency doubled to $\omega_S \approx 2\omega_Q$ and generate the two-photon stabilization drive with the IQ mixer. Finally, the last one is mixed with

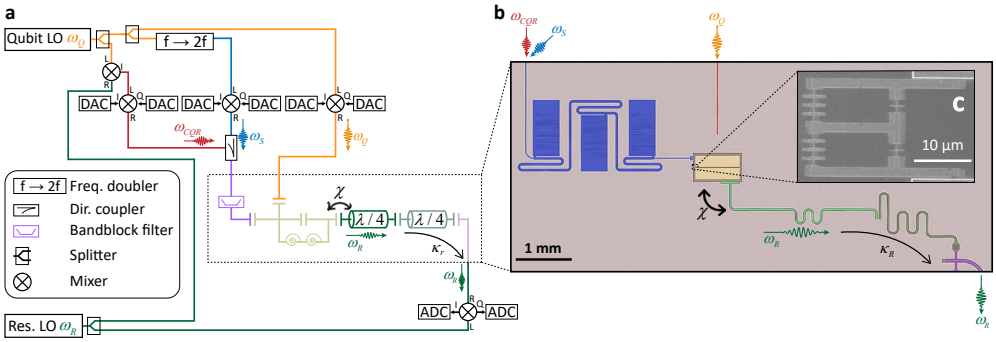

Fig. 1 Device and hardware. **a** Simplified wiring diagram of the chip and the measurement hardware, where the digital-to-analog converters (DACs) are implemented by an arbitrary waveform generator (AWG), and the analog-to-digital converters (ADCs) are implemented by an Alazar sampling card. **b** False-color micrograph of the Kerr-cat qubit device, where the SNAIL nonlinear resonator (yellow) is coupled to a readout resonator (dark green) with its Purcell filter (light green) for quantum nondemolition readout. A weakly coupled control port (orange) delivers the single-photon drive, and a strongly coupled pump port with a bandblock filter (purple) delivers the two-photon stabilization drive and cat-qubit readout drive with suppressed Purcell decay. **c** The scanning electron microscope picture of the two SNAILs.

the readout LO to generate the signal at the cat-qubit readout frequency $\omega_{CQR} \approx \omega_R - \omega_S/2$. The two-photon stabilization drive and the cat-qubit readout drive are both connected to the strongly coupled port (purple) of the device through a directional coupler.

The parameters of the device and the calibration/estimation methods are described in Tab. 1.

Table 1 Device Parameters and Calibration Methods

Parameter	Value	Methods
SNAIL oscillator frequency ω_Q	$2\pi \times 5.9$ GHz	two-tone spectroscopy
SNAIL oscillator Kerr K	$2\pi \times 1.2$ MHz	two-tone spectroscopy
SNAIL large junction E_J	$2\pi \times 263.2$ GHz	room-temp. resistance msmt.[2]
SNAIL small-to-large junction ratio β	0.1	room-temp. resistance msmt.[2]
SNAIL oscillator charge energy E_c	$2\pi\times$ 118 MHz	finite-element-method simulation
SNAIL oscillator relaxation time T_1	40 μs	time-domain coherence msmt.
SNAIL oscillator dephasing time T_2	3.2 μs	time-domain Ramsey msmt.[3]
Readout resonator frequency Ω_R	$2\pi\times$7.1 GHz	microwave reflectrometry
Readout resonator relaxation rate κ_R	$2\pi\times$0.4 MHz	microwave reflectrometry
Readout resonator dispersive shift χ	$2\pi\times$40 kHz	time-domain spectroscopy

2 KCQ Hamiltonian Parameter Calibration

The KCQ Hamiltonian consists of three parameters: the detuning $\Delta = \omega_Q - \omega_S/2$, two-photon stabilization drive strength ϵ_2 and Kerr coefficient K. The parameters are extracted from a series of measurements. Without losing generality, we can set ϵ_2 to be real, and the two-photon stabilization drive frequency ω_S is known from the hardware.

We first extract the KCQ nonlinear oscillator parameters without the two-photon stabilization drive, i.e. $\epsilon_2 = 0$. The KCQ nonlinear oscillator frequency $\omega_Q = \omega_{01}$ is the transition frequency between $|0\rangle$ and $|1\rangle$, determined using standard two-tone spectroscopy[4]. The Kerr nonlinearity is then extracted by preparing the nonlinear oscillator in the first excited states $|1\rangle$ followed by a similar two-tone spectroscopy. where we observed two peaks corresponding to the $|1\rangle \rightarrow |0\rangle$ transition with frequency ω_{01} and $|1\rangle \rightarrow |2\rangle$ transition with frequency $\omega_{12} = \omega_{01} - 2K$, which allows us to extract the Kerr nonlinearity $K = 1.2$ MHz, as shown in Fig. 2a.

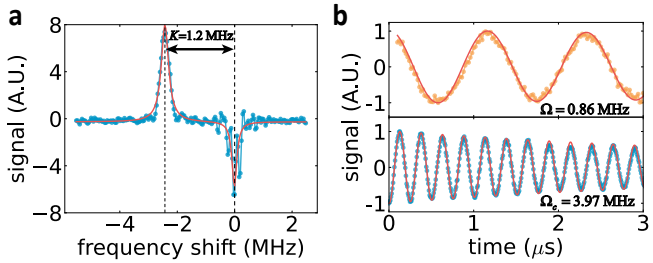

Fig. 2 KCQ Hamiltonian calibration. **a** Calibration of the Kerr nonlinearity. **b** Calibration of the two-photon stabilization drive.

Subsequently, we apply the two-photon stabilization drive to create cat states in the SNAIL nonlinear oscillator, and extract the value of ϵ_2. With the two-photon stabilization drive, the KCQ Hamiltonian supports cat states $|C_\alpha^\pm\rangle \propto |+\alpha\rangle \pm |-\alpha\rangle$ with mean photon number $|\alpha|^2 = (\epsilon_2 + \Delta/2)/K$. Because K and Δ are already calibrated, we only need to calibrate $|\alpha|^2$. As mentioned in reference[1, 5], a single photon drive $H_d = \frac{\Omega}{2}\hat{a}^\dagger + \frac{\Omega^*}{2}\hat{a}$ induces a transition between the two cat states with the rate $\Omega_c = 2\mathrm{Re}[\Omega]\alpha$ with $\epsilon_2 > 0$. Conversely, without the two-photon stabilization drive ($\epsilon_2 = 0$), the same drive can induce the transition between $|0\rangle$ and $|1\rangle$ states of the nonlinear oscillator with the rate Ω. Therefore, by tuning the phase of the single photon drive to make ϵ_1 real and measuring the two transition rates, we can extract, $\alpha = \Omega_c/(2\mathrm{Re}[\Omega])$, as shown in Fig. 2b.

3 KCQ Hamiltonian and Eigenstates

The KCQ Hamiltonian is engineered through a superconducting nonlinear resonator under a strong two-photon stabilization drive. The SNAILs in the resonator provide the nonlinear potential

$$U_{\mathrm{SNAIL}}(\phi) = -\beta E_J \cos\phi - 3E_J \cos\left(\frac{\phi_{\mathrm{ext}} - \phi}{3}\right), \tag{1}$$

where $E_J/\hbar = 2\pi \times 263.2$ GHz is the Josephson energy of the large junction in SNAILs, $\beta = 0.1$ is Josephson energy ratio between the small and large junctions, ϕ_{ext} is the scaled external magnetic flux threading the SNAIL loop, and ϕ is the associated superconducting phase across each SNAIL.

For a fixed external flux, by Taylor expanding the potential energy up to the fourth order,

$$U_{\mathrm{SNAIL}}(\phi) \approx U_{\mathrm{SNAIL}}(\phi_{\mathrm{min}}) + \sum_{k=2}^{4} g_k (\phi - \phi_{\mathrm{min}})^k, \tag{2}$$

one can observe that the SNAIL offers both non-zero third-order and fourth-order nonlinearities necessary for engineering the KCQ Hamiltonian. Under a two-photon stabilization drive, applying the rotating wave approximation in the rotating frame yields the effective Hamiltonian $\hat{H}_{\mathrm{KCQ}}$ shown in the main text. Without loss of generality, the two-photon stabilization drive will be assumed to be in-phase, i.e. $\epsilon_2 \in \mathbb{R}$.

To analyze the eigenenergy and eigenstates of this Hamiltonian, a displacement transformation $\hat{D}(\alpha)$ is introduced to obtain the corresponding Hamiltonian in the displacement frame written as

$$\hat{H}_{\mathrm{KCQ_{disp}}} = E + \Lambda a^\dagger + \Lambda^* a + \tilde{\Delta} a^\dagger a + \tilde{\epsilon}_2 (a^{\dagger 2} + a^2) + \Gamma a^{\dagger 2} a + \Gamma^* a^\dagger a^2 - K a^{\dagger 2} a^2, \tag{3}$$

where the coefficients are given by

$$E = \Delta|\alpha|^2 - K|\alpha|^4 + \epsilon_2(\alpha^2 + \alpha^{*2}), \tag{4a}$$
$$\Lambda = -\Delta\alpha + 2K|\alpha|^2\alpha^* - 2\epsilon_2\alpha^*, \tag{4b}$$
$$\tilde{\Delta} = \Delta - 4K|\alpha|^2, \tag{4c}$$
$$\tilde{\epsilon}_2 = -K\alpha^2 + \epsilon_2, \tag{4d}$$
$$\Gamma = -2K\alpha. \tag{4e}$$

With a suitable choice of $\alpha = \sqrt{(\epsilon_2 + \Delta/2)/K}$, the single-photon drive terms are canceled out (i.e. $\Lambda = 0$), and the displaced Hamiltonian can be written as

$$\hat{H}_{\mathrm{KCQ_{disp}}} = H_0 + H_1, \tag{5a}$$
$$H_0 = \frac{(\Delta/2 + \epsilon_2)^2}{K} - (4\epsilon_2 + \Delta)\, a^\dagger a, \tag{5b}$$
$$H_1 = -\frac{1}{2}\Delta(a^{\dagger 2} + a^2) - (2\epsilon_2 + \Delta)(a^{\dagger 2} a + a^\dagger a^2) - K a^{\dagger 2} a^2, \tag{5c}$$

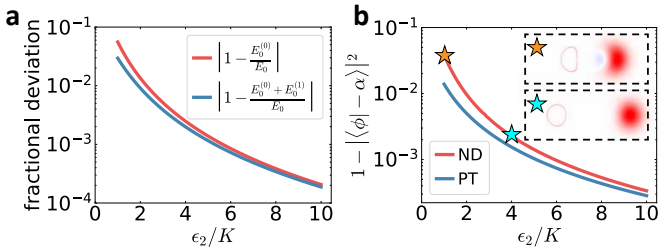

Fig. 3 Detuned-KCQ ground state and its energy with $\Delta = 2K$. **a** The fractional deviation of the ground state energy estimated by the unperturbed Hamiltonian and perturbation theory. **b** The difference between the coherent state and the ground state of the detuned-KCQ Hamiltonian calculated by numerical diagonalization (ND) and perturbation theory (PT).

where the eigenstates and energies of H_0 are Fock states $|n\rangle$ with energy $E_n^{(0)} = (\Delta/2+\epsilon_2)^2/K - (4\epsilon_2+\Delta)\,n$, and H_1 is treated as a perturbation as long as its energy scale is much smaller than the energy gap of the unperturbed system ($|\epsilon_2| \gg |K|, |\Delta/2|$).

Firstly, the perturbed ground state energy is estimated as

$$\tilde{E}_0 = E_0^{(0)} + E_0^{(1)} + \ldots = \frac{(\Delta/2+\epsilon_2)^2}{K} + \frac{\Delta^2 K}{(4\epsilon_2+\Delta)^2} + \ldots, \tag{6}$$

As shown in Fig. 3, we plot the fractional deviation of the estimated ground state energy ($\tilde{E}_0$) from the exact ground state energy (E_0) given by the numerical diagonalization with various two-photon stabilization drive strength. In the regime of interest where $\Delta/K \sim 2$ and $\epsilon_2/K \sim 1-10$, the unperturbed ground state energy $E_0^{(0)}$ matches the exact ground state energy with less than 5% deviation, which is further improved slightly by the perturbation theory.

Secondly, the perturbed ground state (up to the first order) is given by

$$|\psi_0\rangle = \mathcal{N}\left(|0\rangle - \frac{\sqrt{2}\Delta}{4(4\epsilon_2+\Delta)}|2\rangle\right), \tag{7}$$

where the perturbation introduces the occupation beyond the unperturbed ground states, and $\mathcal{N}$ is the normalization factor. After returning to the undisplaced frame, the ground state ends up approximately to the coherent state shown in

$$|\phi\rangle = \hat{D}^\dagger(\alpha)|\psi_0\rangle = \mathcal{N}\left(|-\alpha\rangle - \frac{\sqrt{2}\Delta}{4(4\epsilon_2+\Delta)}\hat{D}^\dagger(\alpha)|2\rangle\right) \approx |-\alpha\rangle. \tag{8}$$

The difference between the coherent state $|-\alpha\rangle$ and the ground state $|\phi\rangle$ of the detuned-KCQ when $\Delta = 2K$ is shown in Fig. 3. The Wigner functions of the ground states when $\epsilon_2/K = 1$ and $\epsilon_2/K = 4$ are also plotted in the inset indicated by the orange and blue stars. Both the results from perturbation theory and numerical diagonalization indicate the rapidly decreasing difference between the coherent state and the detuned-KCQ ground state. At the operating point in this work, such a difference is below 0.3%.

4 Device Fabrication

The device in this work is based on superconducting circuits patterned on an intrinsic silicon (Si) wafer with a resistivity $\rho \geq 10\text{k}\Omega \cdot \text{cm}$. The fabrication process is briefly depicted in the flow chart shown in Fig. 4a. Before the metal deposition, the wafer is cleaned by Piranha solutions ($H_2SO_4 + H_2O_2$) and hydrofluoric acid (HF) to remove the organic contamination and silicon oxide on the surface. The wafer is then transferred to a vacuum box to a Kert J. Lesker sputtering tool for niobium (Nb) deposition. By adjusting the sputtering temperature and pressure, a uniform niobium layer with compressive stress and high superconducting transition temperature[6] is sputtered onto the wafer. The superconducting transition temperature of the film is measured to be 8.94 K, as shown in Fig. 4b. The large structures, including the microwave buses, filter, quarter-wavelength resonators and capacitor pads, are patterned on the Nb film using photolithography and reactive ion etching (RIE). After a second cleaning process with HF to further remove oxides on Si and Nb surfaces, the Josephson junctions are defined with e-beam lithography (EBL) and bridge-free two-angle shadow evaporation of aluminum (Al) films[7]. Electrical contact between the Al Josephson junctions and the Nb capacitor pads is formed by the bandaid process with argon ion-milling[8]. Once diced, the device is packaged into a oxygen-free copper box for testing in the dilution refrigerator.

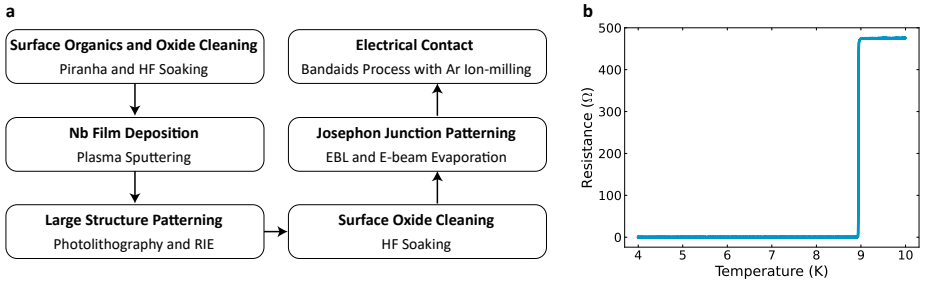

Fig. 4 Fabrication and film quality. **a** Flow chart of the device fabrication process. **b** Measurement of the superconducting transition temperature of the Nb film.

5 GST Circuit Design

GST is a self-consistent calibration free protocol for characterizing the noisy implementation of a informationally complete set of quantum gates[9–11]. GST can estimate the Pauli transfer matrix (PTM) of quantum gates in a SPAM-free manner, and is capable of fitting models with physical constraints such as completely positive, trace preserving (CPTP) constraints[9–11]. This technique has been applied to various platforms of quantum computing, including ion traps[12], spin qubits[13, 14] and superconducting circuits[15]. GST usually executes a set of circuits that consist of a state preparation and readout sequence (*fiducials*) and repeated sequences of gate operations (*germs*) that amplify specific types of error [9, 16].

Because the local gates of KCQ are the discrete $X(\pi/2)$ gate and continuous $Z(\theta)$ gates, we construct the informationally complete set of quantum gates as $\{X(\pi/2), Z(\pi/2), Y(\pi/2)\}$, where the $Y(\pi/2)$ gate is complied using local gates as $X(\pi)Z(\pi/2)X(\pi/2)Z(\pi/2)$. Each GST circuit has the form $F_iG^lF_j$, where F_i and F_j are *fiducial sequences*, G is a *germ* sequence, and l is the maximum integer such that the length of G^l is at most some maximum length L. Using the pyGSTi python package[17], we generate the GST circuits which have a germ set with 10 germs of maximum length 5. The fiducials and germs are shown in Tab. 2.

Table 2 Gate Set Tomography Germs and Fiducials

Germs	$Z(\pi/2), X(\pi/2), Y(\pi/2), Y(\pi/2)X(\pi/2), X(\pi/2)Z(\pi/2),$ $Y(\pi/2)Z(\pi/2), Y(\pi/2)X(\pi/2)X(\pi/2)Z(\pi/2),$ $Y(\pi/2)Y(\pi/2)Y(\pi/2)Z(\pi/2), X(\pi/2)Z(\pi/2)Y(\pi/2)Z(\pi/2)Z(\pi/2),$ $X(\pi/2)X(\pi/2)X(\pi/2)Z(\pi/2)$
Preparation Fiducials	$X(\pi/2), Y(\pi/2), X(\pi/2)X(\pi/2)$, no gates
Measurement Fiducials	$X(\pi/2), Y(\pi/2), X(\pi/2)X(\pi/2)$, no gates

We perform GST with 800 circuits of maximum lengths $L \in \{0, 1, 2, 4, 8, 16, 32, 64, 128\}$ and each circuit is implemented with 1024 shots to obtan the statistics of the measurement results. The process matrices and error generators of $X(\pi/2)$ and $Z(\pi/2)$ gates are extracted by fitting the measurement results to a model with CPTP constraints.

However, the uncertainty of the extracted Pauli X and Pauli Y errors from GST is very large due to the shallow depth of the GST circuits (128 at maximum), which hinders the exact characterization of the noise-bias. Therefore, we employ the DRB protocol with a maximum circuit depth of 2000 to explore the noise structure of KCQ and demonstrate that the performance of detuned-KCQ crosses the fault-tolerant threshold of the XZZX surface code[18, 19].

6 $\mathbb{D}_8$ Dihedral Group Randomized Benchmarking Design

The bit-flip error and phase-flip error, as well as the noise bias are extracted by the DRB protocol introduced in references[19, 20] with a scaling factor to compensate the effect of noise-free $X(\pi)$ gate. We will describe the protocol and illustrate the extraction of the scaling factor by numerical simulations.

The protocol consists of two modified RB sequences labeled by $b = 1$ and 2, shown in Fig. 5a and Fig. 5b, which prepare and measure the qubit along Z and X axis, respectively. The random gates in RB sequences consist of a gate P sampled from the single qubit Pauli group $\mathbb{P}$, followed by n gates D_k sampled from the $\mathbb{D}_8$ dihedral group, and a final gate $D_{n+1} = (D_n...D_2D_1)^{-1}$ to reverse the states. The bit-flip error and phase-flip error are extracted by fitting the character-weighted survival probability $S_b(n)$ (shown in Eq. 9) to an exponential function.

$$S_b(n) := \mathop{\mathsf{E}}_{\substack{P\in\mathbb{P}\\ U_1\cdots U_n\in\mathbb{D}_8}} \left[\chi_b^*(P)\,\Gamma_{\{U_i\}}\right] \tag{9}$$

Here, $\Gamma_{\{U_i\}}$ represents the expectation value of the measurement after applying a sample of RB sequences, while $\mathsf{E}[\cdot]$ denotes the average over all samples of gates. A few typical fitting plots are shown in Fig. 5c and Fig. 5d.

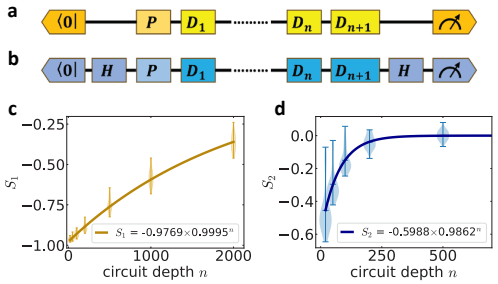

Fig. 5 DRB survival probability fitting. Circuits and fitting curve examples of the exponential decay in the $\mathbb{D}_8$ dihedral randomized benchmarking protocol when **a, c** preparing and measuring the states in Z axis, and **b, d** preparing and measuring the states in X axis.

The scaling factor between the errors of $Z(\theta)$ rotations and the extracted errors from DRB protocol is derived by numerical simulation with qiskit[21] package. We introduce various phase-flip errors $p_{\text{pf, real}}$ ranging from 0 to 3% and bit-flip errors $p_{\text{bf, real}} = 0.02p_{\text{pf, real}}$ to $Z(\theta)$ rotations, while keeping the $X(\pi)$ gate noise-free, and then simulate the DRB experiments to extract the bit-flip $p_{\text{pf, extracted}}$ and phase-flip errors $p_{\text{pf, extracted}}$. As shown in Fig. 6, the extracted errors are proportional to the errors on the $Z(\theta)$ rotations. By fitting the simulation results with a linear function, we extracted the scaling factor between them, where $p_{\text{pf, real}} = 1.02p_{\text{pf, extracted}}$ and $p_{\text{bf, real}} = 1.07p_{\text{bf, extracted}}$.

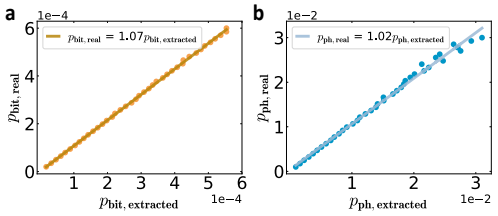

Fig. 6 Scaling factor **a** between the extracted and real bit-flip errors, and **b** between the extracted and real phase-flip errors

7 Description and Analysis of the Error Channels

We model the error channels of KCQ as a combination of coherent Pauli rotation errors and incoherent stochastic Pauli errors described by a Pauli transfer matrix

$\mathcal{E} = e^{\mathbf{L}}$ with the generator $\mathbf{L} = h_x\mathbf{H_x} + h_y\mathbf{H_y} + h_z\mathbf{H_z} + p_x\mathbf{P_x} + p_y\mathbf{P_y} + p_z\mathbf{P_z}$. The coherent components in the error generator are defined in Eq. 10, and the incoherent components are defined in Eq. 11.[22, 23]

$$H_x = \begin{pmatrix} 0 & 0 & 0 & 0 \\ 0 & 0 & 0 & 0 \\ 0 & 0 & 0 & -1 \\ 0 & 0 & 1 & 0 \end{pmatrix}, H_y = \begin{pmatrix} 0 & 0 & 0 & 0 \\ 0 & 0 & 0 & 1 \\ 0 & 0 & 0 & 0 \\ 0 & -1 & 0 & 0 \end{pmatrix}, H_z = \begin{pmatrix} 0 & 0 & 0 & 0 \\ 0 & 0 & -1 & 0 \\ 0 & 1 & 0 & 0 \\ 0 & 0 & 0 & 0 \end{pmatrix} \tag{10}$$

$$P_x = \begin{pmatrix} 0 & 0 & 0 & 0 \\ 0 & 0 & 0 & 0 \\ 0 & 0 & -2 & 0 \\ 0 & 0 & 0 & -2 \end{pmatrix}, P_y = \begin{pmatrix} 0 & 0 & 0 & 0 \\ 0 & -2 & 0 & 0 \\ 0 & 0 & 0 & 0 \\ 0 & 0 & 0 & -2 \end{pmatrix}, P_z = \begin{pmatrix} 0 & 0 & 0 & 0 \\ 0 & -2 & 0 & 0 \\ 0 & 0 & -2 & 0 \\ 0 & 0 & 0 & 0 \end{pmatrix} \tag{11}$$

In the limit of small errors, we can expand the Pauli transfer matrix as $\mathcal{E} = 1 + \mathbf{L} + 0.5\mathbf{L}^2 + o(\mathbf{L}^3)$ in Eq. 12 up to $O(p_m), O(h_n^2)$ with $m, n \in \{x, y, z\}$ and $p = p_x + p_y + p_z$, as shown below

$$\begin{pmatrix} 0 & 0 & 0 & 0 \\ 0 & 1-2(p_y+p_z)-\frac{1}{2}(h_y^2+h_z^2) & -h_z(1+p)+h_xh_y & h_y(1+p)+2h_xh_z \\ 0 & h_z(1+p)+h_xh_y & 1-2(p_x+p_z)-\frac{1}{2}(h_x^2+h_z^2) & -h_x(1+p)+h_yh_z \\ 0 & -h_y(1+p)+h_xh_z & h_x(1+p)+h_yh_z & 1-2(p_x+p_y)-\frac{1}{2}(h_x^2+h_y^2) \end{pmatrix} \tag{12}$$

The coherent error manifests as the off-diagonal elements of the Pauli transfer matrix, which can be effectively removed by the Pauli twirling process. The Pauli twirling process randomly insert Pauli gates $P \in \mathbb{P}$ while compiling circuits, and all the Pauli gates can be executed with error-free virtual X gate, high-fidelity bias-preserving Z gate or their combination. Therefore, Pauli twirled error channels introduces minimal extra noise with preserved the noise-bias property, and are reported to be statistically the same as the full error channels in `XZZX` surface code[18].

The Pauli transfer matrix of the error process after Pauli twirling process reduced to that of a Pauli stochastic error channel shown in Eq. 13,

$$\mathcal{E} = \begin{pmatrix} 0 & 0 & 0 & 0 \\ 0 & 1-2(p'_y+p'_z) & 0 & 0 \\ 0 & 0 & 1-2(p'_x+p'_z) & 0 \\ 0 & 0 & 0 & 1-2(p'_x+p'_y) \end{pmatrix} \tag{13}$$

where the associated stochastic Pauli errors are $p'_m = p_m + 0.25h_m^2, m \in \{x, y, z\}$. Even with the highest coherent error rate, $h_x = 0.0038 \pm 0.002$, of the bias-preserving $Z(\pi/2)$ gate estimated from GST, the contribution of stochastic Pauli X error from this coherent error is $3.61 \times 10^{-6} \pm 3 \times 10^{-6}$, which is two orders or magnitude smaller than the stochastic Pauli X error. Therefore, the effects of coherent errors are negligible.

References

[1] Hajr, A. *et al.* High-coherence kerr-cat qubit in 2d architecture. *Phys. Rev. X* **14**, 041049 (2024).

[2] Ambegaokar, V. & Baratoff, A. Tunneling between superconductors. *Phys. Rev. Lett.* **10**, 486 (1963).

[3] Steck, D. A. *Quantum and atom optics* (2007).

[4] Krantz, P. *et al.* A quantum engineer's guide to superconducting qubits. *Appl. Phys. Rev.* **6** (2019).

[5] Grimm, A. *et al.* Stabilization and operation of a kerr-cat qubit. *Nature* **584**, 205–209 (2020).

[6] Kuroda, K. & Yuda, M. Niobium-stress influence on nb/al-oxide/nb josephson junctions. *J. Appl. Phys.* **63**, 2352–2357 (1988).

[7] Lecocq, F. *et al.* Junction fabrication by shadow evaporation without a suspended bridge. *Nanotechnology* **22**, 315302 (2011).

[8] Qing, B. *et al.* Broadband coplanar-waveguide-based impedance-transformed josephson parametric amplifier. *Phys. Rev. Res.* **6**, L012035 (2024).

[9] Nielsen, E. *et al.* Gate set tomography. *Quantum* **5**, 557 (2021).

[10] Brieger, R., Roth, I. & Kliesch, M. Compressive gate set tomography. *PRX quantum* **4**, 010325 (2023).

[11] Cao, S. *et al.* Efficient characterization of qudit logical gates with gate set tomography using an error-free virtual z gate model. *Phys. Rev. Lett.* **133**, 120802 (2024).

[12] Blume-Kohout, R. *et al.* Robust, self-consistent, closed-form tomography of quantum logic gates on a trapped ion qubit. *preprint arXiv:1310.4492* (2013).

[13] Stemp, H. G. *et al.* Tomography of entangling two-qubit logic operations in exchange-coupled donor electron spin qubits. *Nat. Commun.* **15**, 8415 (2024).

[14] Bartling, H. *et al.* Universal high-fidelity quantum gates for spin-qubits in diamond. *preprint arXiv:2403.10633* (2024).

[15] Hashim, A. *et al.* Benchmarking quantum logic operations relative to thresholds for fault tolerance. *npj Quantum Inf.* **9**, 109 (2023).

[16] Nielsen, E., Blume-Kohout, R. J., Rudinger, K. M., Proctor, T. J. & Saldyt, L. Python gst implementation (pygsti) v. 0.9. Tech. Rep., Sandia National Lab.(SNL-NM), Albuquerque, NM (United States) (2019).

[17] Nielsen, E., Blume-Kohout, R. J., Rudinger, K. M., Proctor, T. J. & Saldyt, L. Python gst implementation (pygsti) v. 0.9. Tech. Rep., Sandia National Lab.(SNL-NM), Albuquerque, NM (United States) (2019).

[18] Darmawan, A. S., Brown, B. J., Grimsmo, A. L., Tuckett, D. K. & Puri, S. Practical quantum error correction with the xzzx code and kerr-cat qubits. *PRX Quantum* **2**, 030345 (2021).

[19] Claes, J. & Puri, S. Estimating the bias of cx gates via character randomized benchmarking. *PRX Quantum* **4**, 010307 (2023).

[20] Carignan-Dugas, A., Wallman, J. J. & Emerson, J. Characterizing universal gate sets via dihedral benchmarking. *Phys. Rev. A* **92**, 060302 (2015).

[21] Wille, R., Van Meter, R. & Naveh, Y. *Ibm's qiskit tool chain: Working with and developing for real quantum computers*, 1234–1240 (2019).

[22] Blume-Kohout, R. *et al.* A taxonomy of small markovian errors. *PRX Quantum* **3**, 020335 (2022).

[23] Carignan-Dugas, A., Ranu, S. K. & Dreher, P. Estimating coherent contributions to the error profile using cycle error reconstruction. *Quantum* **8**, 1367 (2024).